PNAS RESEARCH ARTICLE | PHARMACOLOGY

# Cryo-EM structures of human GPR34 enable the identification of selective antagonists

Anjie Xia[a,b,1], Xihao Yong[a,1], Changbin Zhang[a,1], Guifeng Lin[a,1], Guowen Jia[a,1], Chang Zhao[a,1], Xin Wang[a,1], Yize Hao[c,d,1], Yifei Wang[a], Pei Zhou[e], Xin Yang[a], Yue Deng[a], Chao Wu[a], Yujiao Chen[a], Jiawei Zhu[a], Xiaodi Tang[a], Jingming Liu[a], Shiyu Zhang[a], Jiahao Zhang[a], Zheng Xu[a], Qian Hu[a], Jinlong Zhao[a], Yuting Yue[c,d], Wei Yan[a], Zhaoming Su[a], Yuquan Wei[a], Rongbin Zhou[c,d,2], Haohao Dong[a,2], Zhenhua Shao[a,f,2], and Shengyong Yang[a,f,2]

Edited by Robert Lefkowitz, HHMI, Durham, NC; received May 19, 2023; accepted August 4, 2023

**GPR34 is a functional G-protein-coupled receptor of Lysophosphatidylserine (LysoPS), and has pathogenic roles in numerous diseases, yet remains poorly targeted. We herein report a cryo-electron microscopy (cryo-EM) structure of GPR34 bound with LysoPS (18:1) and $G_i$ protein, revealing a unique ligand recognition mode with the negatively charged head group of LysoPS occupying a polar cavity formed by TM3, 6 and 7, and the hydrophobic tail of LysoPS residing in a lateral open hydrophobic groove formed by TM3-5. Virtual screening and subsequent structural optimization led to the identification of a highly potent and selective antagonist (YL-365). Design of fusion proteins allowed successful determination of the challenging cryo-EM structure of the inactive GPR34 complexed with YL-365, which revealed the competitive binding of YL-365 in a portion of the orthosteric binding pocket of GPR34 and the antagonist-binding-induced allostery in the receptor, implicating the inhibition mechanism of YL-365. Moreover, YL-365 displayed excellent activity in a neuropathic pain model without obvious toxicity. Collectively, this study offers mechanistic insights into the endogenous agonist recognition and antagonist inhibition of GPR34, and provides proof of concept that targeting GPR34 represents a promising strategy for disease treatment.**

GPCR | GPR34 | cryo-EM | antagonist

## Significance

GPR34 is a Lysophosphatidylserine (LysoPS) receptor with pathogenic roles in numerous diseases. In this work, we solved the cryo-EM (cryo-electron microscopy) structures of both activated and inactivated GPR34. By utilizing the solved cryo-EM structure of GPR34, we identified a potent and selective GPR34 antagonist and demonstrated its effectiveness in the neuropathic pain model. Our investigation offers mechanistic insights into the endogenous agonist recognition and antagonist inhibition of GPR34, and provide proof-of-concept that targeting GPR34 represents a promising strategy for disease treatment.

Lysophosphatidylserine (LysoPS) is an emerging bioactive lipid mediator generated by enzymatic hydrolysis of membrane phospholipid, phosphatidylserine (PS) (1). LysoPS is an amphipathic molecule with a phosphoserine group as the hydrophilic head, a fatty acid [e.g., oleic acid (18:1)] as the hydrophobic tail, and a glycerol moiety linking the two parts (Fig. 1*A*). LysoPS can signal through specific cell-surface G-protein-coupled receptors (GPCRs), participating in the regulation of some important physiological processes, such as, immunomodulation (2, 3) and microglia colonization (4). Recent studies have also revealed its pathological role in several diseases, such as neuropathic pain (5) and autoimmune diseases (6, 7). Currently, three GPCRs, GPR34, P2Y10, and GPR174, have been identified as LysoPS cognate functional receptors (8–10).

GPR34 is the first discovered cell-surface receptor of LysoPS, which is highly expressed in immune cells, such as microglia and mast cells (8, 11). Increasing evidence shows that GPR34 has pathogenic roles in numerous diseases (12). For example, GPR34 was found to be overexpressed in the microglia of spinal dorsal horn after sensory nerve injury, which contributes to neuropathic pain, and GPR34 gene deletion significantly reduced this kind of neuropathic pain (5). Moreover, GPR34 is also implicated in several types of cancer, including gastric cancer (13), colorectal cancer (14, 15), and cervical cancer (16). Interestingly, GPR34-knock-out mice showed no obvious abnormalities in broad phenotypical screens in respect to anatomy, histology, laboratory chemistry, and behavior (17). All these findings suggest that GPR34 is an attractive therapeutic target for related diseases, and antagonists of GPR34 may be potential agents for the treatment of related diseases.

Currently, a series of studies that focus on the optimization of LysoPS as agonists to improve its potency and selectivity have been reported (18–21). However, there is still a lack of potent and selective GPR34 antagonists, and the structural organization and signaling mechanisms of GPR34 are largely unknown. In this investigation, we identify a highly potent and selective antagonist of GPR34 (YL-365), and report cryo-electron microscopy (cryo-EM) structures of both activated GPR34 [bound with LysoPS (18:1) and $G_i$] and inactivated GPR34 (complexed with YL-365). These structures reveal unique molecular mechanisms underlying the endogenous ligand recognition and antagonist inhibition of GPR34. Moreover, we demonstrate the effectiveness of antagonist YL-365 in a mouse model of neuropathic pain, highlighting a great potential of targeting GPR34 in disease treatment.

Author contributions: S.Y., Z. Shao, H.D., and R.Z. designed research; A.X., X.Y., C. Zhang, G.L., G.J., C. Zhao, X.W., Y.H., Y. Wang, P.Z., X.Y., Y.D., C.W., Y.C., J. Zhu, J.L., S.Z., J. Zhang, Z.X., Q.H., J. Zhao, and Y.Y. performed research; S.Y., Z. Shao, H.D., R.Z., A.X., X.Y., C. Zhang, G.L., G.J., C. Zhao, X.W., Y.H., X.T., W.Y., Z. Su, and Y. Wei analyzed data; and S.Y., Z. Shao, H.D., R.Z., A.X., C. Zhang, G.L., C. Zhao, and X.W. wrote the paper.

Competing interest statement: Sichuan University has applied for Chinese patents covering YL-365 and related compounds. Other authors declared no competing interests.

This article is a PNAS Direct Submission.



[1]A.X., X.Y., C. Zhang, G.L., G.J., C. Zhao, X.W., and Y.H. contributed equally to this work.

[2]To whom correspondence may be addressed. Email: zrb1980@ustc.edu.cn, haohaodong@scu.edu.cn, zhenhuashao@scu.edu.cn, or yangsy@scu.edu.cn.

This article contains supporting information online at https://www.pnas.org/lookup/suppl/doi:10.1073/pnas.2308435120/-/DCSupplemental.

Published September 21, 2023.

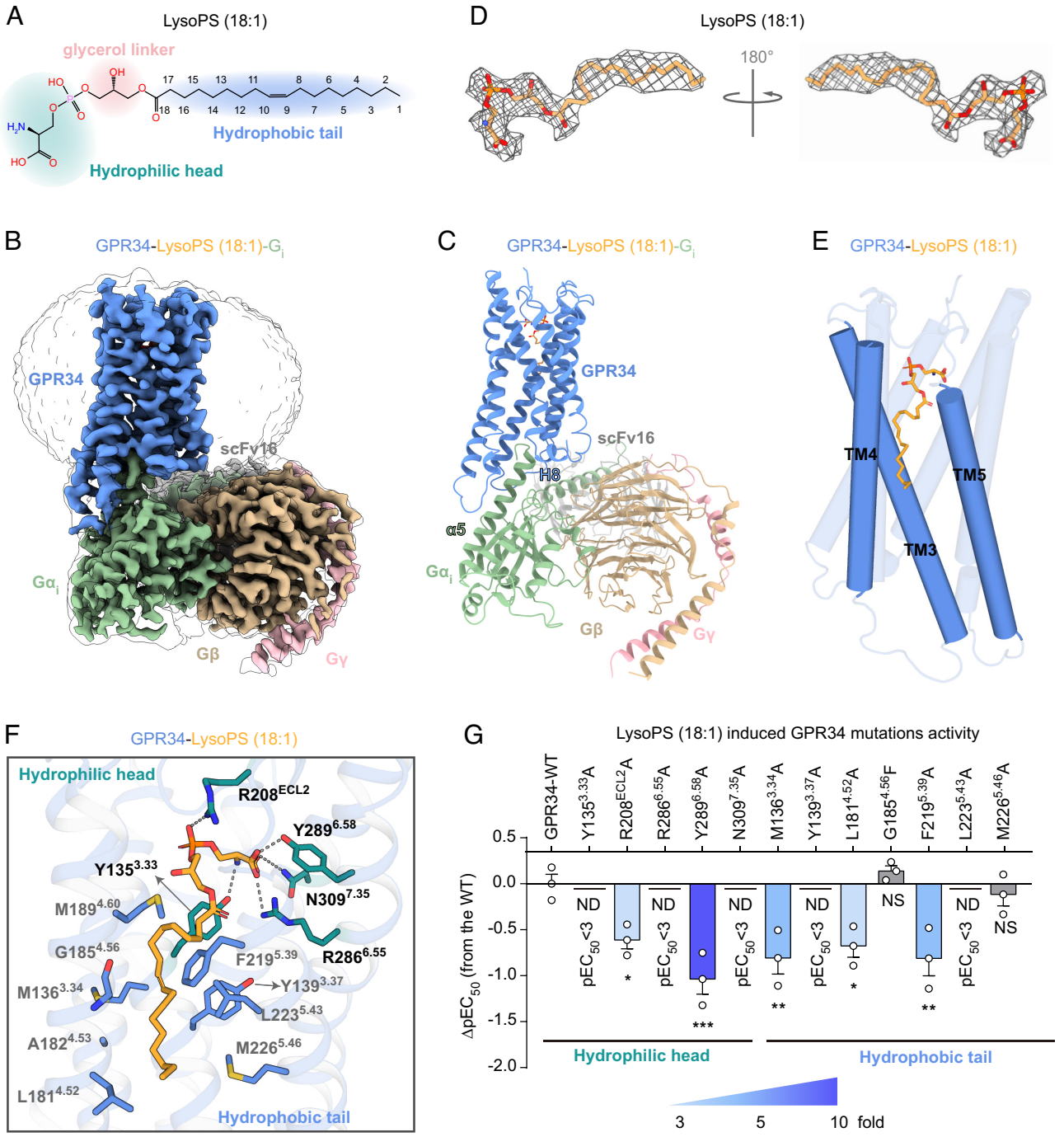


**Fig. 1.** Cryo-EM structure of GPR34-$G_i$ in complex with LysoPS (18:1). (*A*) Chemical structure of LysoPS (18:1). The hydrophilic head, glycerol linker, and hydrophobic tail of LysoPS (18:1) are highlighted with cadet blue, pink, and cornflower blue shading, respectively. (*B* and *C*) The cryo-EM density map (*B*) and model (*C*) of LysoPS (18:1)-bound GPR34-$G_{i1}$ complex. Cornflower blue, GPR34; pale green, $G\alpha_i$; tan, Gβ; pink, Gγ; dark gray, scFv16; bright orange, LysoPS (18:1). (*D*) Cryo-EM density map shown as dark gray meshes allowed unambiguous identification of LysoPS (18:1). The density map of LysoPS (18:1) are depicted at contour level of 0.397. (*E*) Orthogonal view of cartoon model of LysoPS (18:1)-bound GPR34. The hydrophobic tail of LysoPS (18:1) extended toward TM3-TM5. The helical bundle of GPR34 is presented as cylindrical helices. (*F*) Key residues involved in LysoPS (18:1) recognition. The residues in contact with the hydrophilic head of LysoPS (18:1) are colored cadet blue, and those engaged with the hydrophobic tail are colored cornflower blue. Polar interactions are highlighted as gray dashed lines. (*G*) Mutagenesis effects of orthosteric-site residues of GPR34 on their activities in response to LysoPS (18:1) stimulation examined by $G\alpha_{i1}$-$G\gamma_2$ dissociation assay. Bars represent differences in calculated potency ($\Delta pEC_{50}$) for each mutant shown as percentage of the maximum in wild type (WT). The $\Delta pEC_{50}$ values were derived from the dose-dependent curves in *SI Appendix*, Fig. S3 *G* and *H*. Statistical differences between WT and mutants were determined by two-sided, one-way ANOVA with Tukey's test. *$P < 0.05$; **$P < 0.01$; ***$P < 0.001$; ND, not detectable due to low signal; NS, no significant difference. Data are presented as the mean ± SEM of three independent experiments performed in triplicate.

## Results

**Cryo-EM Structure of Activated GPR34-$G_i$ Complex Bound to LysoPS (18:1).** To obtain human GPR34-$G_i$ signal transduction complex, we truncated the N-terminal residues (1 to 38) and C-terminal residues (373 to 381) of the receptor and inserted a fusion protein BRIL (Thermostabilised apocytochrome b562 from Escherichia coli M7W/H102I/R106L) into the N-terminus for expression level improvement. The modified GPR34 and heterotrimeric $G_i$ complex was coexpressed in *Sf9* insect cells, and the complex was assembled under the conditions of endogenous agonist LysoPS (18:1) and apyrase (22). To further enhance complex stability, we

utilized scFv16, which is a single-chain variable fragment derived from a monoclonal antibody that was raised against Rhodopsin-$G_{i1}$ complex (23). Eventually, single-particle cryo-EM analysis of the sample enabled us to obtain nominal global maps at 3.27 Å resolution for structure of LysoPS (18:1)-bound GPR34-$G_i$-scFv16 complex (Fig. 1*B* and *SI Appendix*, Fig. S1 and Table S1).

The overall structure of the GPR34-$G_i$ complex reveals a similar assembly mode as most lipid receptor signaling complexes, such as CB1-$G_i$, S1PR1-$G_i$, and LPAR1-$G_i$ complexes, with Cα atom RMSD values being 0.54 Å, 0.99 Å, and 0.86 Å for the whole complex, respectively, suggesting that the structure of GPR34-$G_i$ complex is active state (*SI Appendix*, Fig. S2 *A–C*). In the final structure model of activated GPR34-$G_i$ in complex with LysoPS (18:1), GPR34 was associated with $G_i$ by its intracellular part to interact with the C-terminus of $G\alpha_i$ (mainly α helix 5, see α5 in Fig. 1*C*). GPR34 itself adopted the canonical seven transmembrane (7TM) bundle of α-helices, with three extracellular loops, three intracellular loops, and a short amphipathic helix 8 (H8) oriented parallel to the membrane (*SI Appendix*, Fig. S2*D*). Of note is that the ECL2 loop was stabilized into a U-shape by forming a disulfide bond between $C204^{ECL2}$ and $C127^{3.25}$ (*SI Appendix*, Fig. S2*E*). The U-shaped ECL2 together with TM3 and TM5-7 likely constitute the orthosteric ligand binding pocket with ECL2 like a cap of the pocket.

**Recognition of the Endogenous LysoPS (18:1) by GPR34.** A well-defined density was clearly observed in the orthosteric site (Fig. 1*D*), which allowed us to unambiguously model the agonist LysoPS (18:1) in the structure with the acyl tail extending into the cleft between TM3-5 (Fig. 1*E*). The complex structure provides signaling mechanism of LysoPS (18:1) action, and helps us understand structure-activity relationship (SAR) of LysoPS analogs. Structurally, LysoPS (18:1) can be divided into three parts: a hydrophilic head, a hydrophobic tail, and a glycerol linker (Fig. 1*A*). When comparing with binding poses of other lipids in receptors, we found that the hydrophilic head of sphingosine 1-phosphate (S1P), lysophosphatidic acid (LPA), and lysophosphatidylcholine (LPC) located close to TM1, TM2, and TM7 in S1PR3 (24), LPAR1 (25), and GPR119 (26) (*SI Appendix*, Fig. S2 *F–H*). However, the hydrophilic head of LysoPS (18:1) occupies the pocket formed by TM3, TM6, and TM7 in GPR34 (*SI Appendix*, Fig. S2 *E* and *F*). Distinct from bending conformation of hydrophobic tails of LPA in LPAR1, the LysoPS (18:1), S1P and LPC adopt extended binding poses in corresponding receptors (24–26)

The hydrophilic head of LysoPS (18:1), consisting of L-serine and phosphodiester, together with the glycerol linker adopts a U-shape and forms a polar interaction network with ECL2, TM3 and TM6/7 (Fig. 1*F*). In particular, the amino group of L-serine forms a hydrogen bond with $Y135^{3.33}$, whereas the carboxyl group was observed to extend toward TM6 and TM7, forming salt bridge or hydrogen bonds with side chains of $R286^{6.55}$, $Y289^{6.58}$, and $N309^{7.35}$, respectively (Fig. 1*F*). Likewise, a similar polar pocket was observed in GPR174, consisting of $R75^{2.60}$, $Y79^{2.64}$, $Y99^{3.33}$, $R156^{4.64}$, $Y246^{6.51}$, and $K257^{6.62}$, accommodating the L-serine moiety of LysoPS (*SI Appendix*, Fig. S3*A*).Previous SAR studies of LysoPS showed that either deletion of the carbonyl oxygen or introduction of a methyl group in the serine moiety substantially reduced the activity of GPR34 and GPR174 (18, 27), which could be due to the breaking of interactions between serine and these residues. Moreover, modification of L-serine by a methyl group to lysophosphatidylthreonine failed to activate GPR34 signaling transduction (18), which might be due to the potential clash between the threonine analogue and the side chain of $Y135^{3.33}$ (*SI Appendix*, Fig. S3*B*). These results indicate that the serine moiety serves as a key determinant role for LysoPS receptor subfamily activation. The phosphate group, a typical character of lysophospholipids (LPLs), is observed to form salt bridge with the side-chain of $R208^{ECL2}$ (Fig. 1*F*). This arrangement placed the side chain of $F205^{ECL2}$ into a classic orthosteric binding pocket (OBP), making direct van der Waals forces with phosphate group of LysoPS (18:1), which in turn prevents the L-serine group from coming near TM1, TM2, and TM7 (*SI Appendix*, Fig. S3*C*).

The glycerol subgroup, another important moiety of LPLs, is packed by $G131^{3.29}$ and $T132^{3.30}$, making direct contacts with TM3 (*SI Appendix*, Fig. S3*D*). Consistent with our structural observation, cyclic substitution of glycerol moiety with tetrahydropyran could restrict the flexibility of LysoPS (18:1) and enhance receptor activation (19). In addition, introduction of methoxy or ethoxy at C2 of glycerol moiety has more selectivity on GPR34 than P2Y10 and GPR174 (21), which is because $G131^{3.29}$ and $T132^{3.30}$ in GPR34 were replaced by bulkier aromatic residues $F^{3.29}$ and $Y^{3.30}$ in GPR174 or P2Y10. (*SI Appendix*, Fig. S3*E*).

The hydrophobic tail of LysoPS (18:1) in the structure of GPR34 exhibits twisted shape conformation with its acyl chain placed into a cleft formed by TM3-5, engaging in extensive hydrophobic contacts with the receptor (Fig. 1*F*). The residues $Y135^{3.33}$, $M136^{3.34}$, and $Y139^{3.37}$ from TM3 make up the back side of the hydrophobic cavity, $M189^{4.60}$, $G185^{4.56}$, $A182^{4.53}$, $L181^{4.52}$ from TM4 and $F219^{5.39}$, $L223^{5.43}$, $M226^{5.46}$ from TM5 define a vertical cavity that could accommodate length of the ligand. It is noteworthy that the lipid tail of LysoPS (18:1) is projected into the laterally open cleft, which is accessible to the environment of lipid bilayer membrane (*SI Appendix*, Fig. S3*F*).

To validate the observed agonist binding modes, we performed a series of mutagenesis studies and cell-based pharmacological assays. Consistent with structural observations, individual alanine mutations of residues $Y135^{3.33}$, $R208^{ECL2}$, $R286^{6.55}$, $Y289^{6.58}$, and $N309^{7.35}$ involved in hydrophilic head recognition reduced LysoPS (18:1)-induced receptor activation. In particular, the GPR34 mutants $Y135^{3.33}$A, $R286^{6.55}$A, and $N309^{7.35}$A nearly abolished receptor activation (Fig. 1*G* and *SI Appendix*, Fig. S3*G* and Table S2). Meanwhile, in hydrophobic binding pocket, alanine substitution of $Y139^{3.37}$ and $L223^{5.43}$ severely impaired the receptor activation simulated by LysoPS (18:1) (Fig. 1*G* and *SI Appendix*, Fig S3*H*). These findings highlight the critical role of the hydrophilic head binding site and the hydrophobic cleft in receptor activation. We next performed a 500 ns MD simulation of GPR34 bound to LysoPS (18:1), which reveals that LysoPS (18:1) binds to the pocket of GPR34 stably (*SI Appendix*, Fig. S3 *I* and *J*).

**Identification of GPR34 Antagonist YL-365.** To obtain antagonists of GPR34, molecular docking–based virtual screening was first carried out with the obtained cryo-EM structure of GPR34. Chemical libraries used in the virtual screening include ZINC database (28) and an in-house database, containing about 8 million drug-like compounds in total. From top ranked compounds in this screening campaign (Fig. 2*A*; details see *SI Appendix, Supplementary Materials and Methods* section), we selected 20 compounds for further bioactivity validation (*SI Appendix*, Table S3). Of them, three compounds showed antagonistic activity and compound D0010242 (Hit-1) is the most active one with a half maximal inhibitory concentration ($IC_{50}$) value of 2.183 μM against GPR34 in the Tango assay (29) (*SI Appendix*, Table S3). Therefore, Hit-1 was chosen for further structural optimization; another reason why we did not choose the other two compounds was because they showed obvious cytotoxicity at 10 μM.

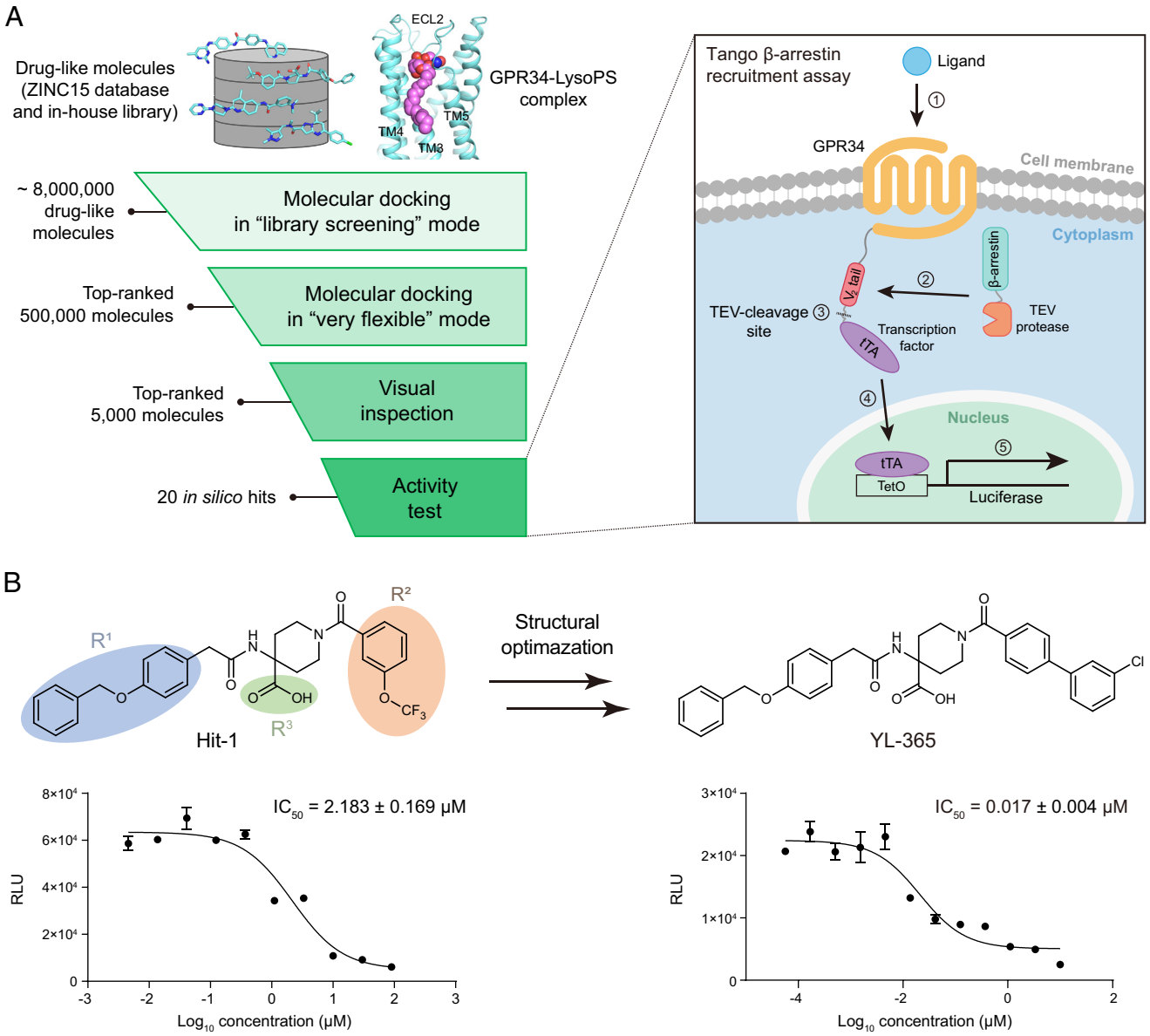


**Fig. 2.** Hit identification and structural optimization. (*A*) Flowchart for the screening process of hit compound (Hit-1). (*B*) Structural optimization of Hit-1 led to the identification of a potent GPR34 antagonist YL-365. Bioactivities of compounds were measured by the Tango assay. Dose–response curves of Hit-1 and YL-365 are shown. $IC_{50}$ values are mean ± SD from three independent experiments.

We then performed structural optimization toward Hit-1 to improve its potency. The structural optimization was focused on three regions: (benzyloxy)phenyl ($R^1$), trifluoromethoxyphenyl ($R^2$), and carboxyl ($R^3$) (Fig. 2*B*). In the first step, we fixed $R^2$ and $R^3$ as their original groups and optimized $R^1$. Shifting the benzyloxy group from paraposition to metaposition or orthoposition substantially reduced the potency (Hit-1 vs C-01 and C-02; *SI Appendix*, Fig. S4), and removing the benzyloxy group from the paraposition evidently decreased the activity (Hit-1 vs. C-03), indicating that substitution at the paraposition other than the metaposition or orthoposition is important for the potency improvement. Various substituents were then used to replace the benzyloxy group at the paraposition. Seven compounds were synthesized. Unfortunately, the potency of these compounds did not exceed that of Hit-1 (C-04 to C-10). In the second step, we optimized $R^2$ with $R^1$ fixed as the optimal group and $R^3$ as its original group. Again, we transferred the -$OCF_3$ group on the benzene ring from metaposition to paraposition or orthoposition. Compound C-11 with paratrifluoromethoxyphenyl at $R^2$ showed obviously improved potency but C-12 with ortho-trifluoromethoxyphenyl did not (*SI Appendix*, Fig. S4). Removing of -$OCF_3$ group also significantly decreased the activity (C-13). These results indicate that the parasubstitution benefits to potency enhancement. Therefore, we used various subgroups on the paraposition and prepared 10 compounds (C-14 to C-23). Nine of them showed antagonistic activity against GPR34 and C-20 (hereafter named as YL-365), bearing a 3-chloro-biphenyl group at $R^2$, showed the highest activity with an $IC_{50}$ value of 17 nM. Third, we fixed $R^1$ and $R^2$ as their optimal groups and optimized $R^3$. The carboxyl group was removed or replaced by methoxycarbonyl, carboxymethyl, carbamoyl, and tetrazolyl (C-24 to C-28). Some of the leading compounds (C-26, C-27) showed antagonistic effect but their potency did not exceed that of YL-365. Overall, the structural optimization and SAR analysis led to the identification of compound YL-365, which showed a low-nanomolar potency (17 nM) against GPR34.

We further tested the activity of YL-365 against GPR174 and P2Y10, as well as other GPCRs, including lipid receptors (LPA receptors, S1P receptors, GPR55, CB1 and CB2), P2Y receptor

($P2Y_{12}R$), chemokine receptor (CXCR5), adenosine receptor ($A_3AR$), Gonadotropin-releasing hormone receptor (GnRH1R), angiotensin receptor (AGTR1), and acetylcholine receptors (CHRM1 and CHRM2). YL-365 did not show activity against all the tested GPCRs (*SI Appendix*, Table S4). We then tested the activity of YL-365 against human protein kinases, which are the most important signaling transduction proteins and participate various physiological and pathological processes. YL-365 did not show any inhibitory effect on a panel of 378 human protein kinases (*SI Appendix*, Table S5). All these data indicate that YL-365 is a selective GPR34 antagonist.

**Cryo-EM Structure of GPR34 Bound to YL-365.** To understand the interaction mode between YL-365 and GPR34, we tried to solve the cryo-EM structure of inactivated GPR34 bound with YL-365. To this end, we engineered the full-length human GPR34 by inserting a thermostable glycogen synthase domain of *Pyrococcus abyssi* (PGS) into ICL3 (30) to mark the orientation of the receptor for cryo-EM identification (*SI Appendix*, Fig. S5*A*). The purified GPR34-PGS was incubated with the antagonist YL-365 in vitro to obtain the inactive form of GPR34 (*SI Appendix*, Fig. S5 *B* and *C*). Single-particle cryo-EM resulted in the three-dimensional reconstruction of GPR34-YL-365 at 3.3 Å resolution (Fig. 3*A*). The high-resolution cryo-EM map allowed unambiguous assignment of the majority of GPR34, except the flexible intracellular loops including N157-I166 of ICL2 and $G242^{5.62}$-$Y261^{6.30}$ (Fig. 3*B* and *SI Appendix*, Fig. S6). Additional density was observed in the orthostatic ligand-binding pocket of GRP34 surrounded by TM3-5, which was modelled as YL-365 (Fig. 3 *A* and *B*). The antagonist orientation was validated by Q-score analysis of 0.45, which is comparable to the average Q-score of models built at such resolution (31).

The overall structure of the inactive GPR34 is similar to that of the active GPR34 (Figs. 1 *B* and *C* and 3 *A* and *B*). A disulfide bond could also be formed between $C204^{ECL2}$ and $C127^{3.25}$ in inactive GPR34 stabilizing the ECL2 in a U-shape, which is highly conserved in class A GPCR superfamily (32) (Fig. 3*C*). The configuration of GPR34 in the GPR34-YL-365 complex shows high homology to the inactive form of P2Y family proteins (12, 33), with RMSD of 1.01 Å, 0.98 Å, 1.23 Å over all Cα atoms when compared with the antagonist-bound $P2Y_1R$ (34), $P2Y_{12}R$ (35) and the classic class A receptor $\beta_2AR$ (36), respectively (*SI Appendix*, Fig. S7*A*). The hallmark of GPCR inactive conformation, the inward incline of the intracellular end of TM6, is observed in the GPR34-YL-365 structure (*SI Appendix*, Fig. S7 *A* and *B*). This rearrangement triggers the closure of the cytoplasmic pocket to prevent the coupling of the receptor with downstream effectors, resulting the inactivated receptor. On the other hand, TM5 and TM4 show distinctiveness from other classic A GPCR structures, with the intracellular tip of TM5 shifted inward and TM4 shifts outward from the center of the 7TM bundles, significantly, providing space for antagonist binding (*SI Appendix*, Fig. S7*B*).

The antagonist YL-365 binds into the lateral open cavity surrounded by TM3-5 and forms extensive hydrophobic interactions within the elongated binding pocket with the helix residues that are distinct from those in GPR174 and P2Y10 (Fig. 3 *C* and *D* and *SI Appendix*, Fig. S7*C*), the nonconservation of residues in the hydrophobic groove formed by TM3-5 may be the major reason leading to the selectivity of YL-365. The 4-benzyloxyphenyl moiety ($R^1$) of YL-365 makes tight hydrophobic interactions with $L181^{4.52}$, $I177^{4.48}$, $I143^{3.41}$ and $F147^{3.45}$, whereas the 3-chloro-biphenyl group ($R^2$) forms hydrophobic interactions with $T132^{3.30}$, $Y135^{3.33}$ and $F219^{5.39}$ (Fig. 3 *D* and *E*). Consistent with the observation in the SAR analysis, substitutions at the metaposition or orthoposition in $R^1$ (benzyloxy, *SI Appendix*, Fig. S4) would cause collision with the surrounding residues (I177 and I143), thus may lead to the reduced potency.

Comparison of GPR34-YL-365 with inactive structures of other class A GPCRs can help us understand mechanistic insights into the conformational rearrangements induced by YL-365 binding. The conserved "toggle switch" $W^{6.48}$ in the class A GPCRs was postulated as the initial step in GPCR activation (37, 38), which is replaced by $F(Y)^{6.48}$ in GPR34 and other P2Y family members (*SI Appendix*, Fig. S7*D*). The different reversals of $F(Y)^{6.48}$ resulting from the binding of ligands of different potencies have been shown to be closely related with the conformational changes of the receptor in the inactivated state (39). Comparison of the antagonist binding mode of GPR34 with carazolol binding in $\beta_2AR$, YL-365 is further away from the "toggle switch" with the shortest distance of 12.7 Å compared with 3.4 Å in $\beta_2AR$. However, it is also observed in the inactive structures of MRS2500-bound $P2Y_1R$ for 18.8 Å and AZD1283-bound $P2Y_{12}R$ for 10.7 Å (*SI Appendix*, Fig. S7*D*). The similarity in the relative displacement of the "toggle switch" residue $F(Y)^{6.48}$ suggests that YL-365 may adopt a mechanism more similar to that of P2Y family-related antagonists to induce conformational rearrangements of the receptor in the inactivated state (34, 35).

To validate the observed antagonist binding mode, we performed a series of mutagenesis studies and cell-based pharmacological assays. Individual alanine mutations of residues $K128^{3.26}$, $Y135^{3.34}$, $Y139^{3.37}$, $L181^{4.52}$, and $E216^{5.36}$, which are the key residues forming the hydrophobic pocket accommodating the antagonist, evidently reduced receptor inhibition by YL-365 (Fig. 3 *D* and *F* and *SI Appendix*, Fig. S7*E*). In particular, $L181^{4.52}$A and $E216^{5.36}$A substantially reduced the potency of YL-365 by approximately 10- to 30-folds. We next performed a 500-ns MD simulation of GPR34 bound to YL-365, which reveals that YL-365 resides in the pocket of GPR34 stably (*SI Appendix*, Fig. S7*F*).

**Comparison of Active/Inactive Structures Reveals the Underlying Mechanism for GPR34 Activation and Antagonist Inhibition.** The endogenous agonist-bound active and antagonist-bound inactive GPR34 structures determined here offer us an opportunity to understand the underlying mechanism for the receptor activation and antagonist inhibition. Superposition of the active and inactive GPR34 structures reveals notable differences in both the extracellular and cytoplasmic regions. When sensing the endogenous agonist LysoPS (18:1), ECL2, the extracellular ends of TM4, TM5, and TM6 in GPR34 shifted inward, shrinking the OBP of receptor (Fig. 4*A*). At the cytoplasmic side, remarkable extension of TM5 and outward movement of TM6 or TM7 were observed, allowing $G_i$-protein coupling (Fig. 4*A* and *SI Appendix*, Fig. S8*A*).

To understand the detailed mechanism of GPR34 activation, we first analyzed the structural changes upon the receptor activation. As is seen in Fig. 4*B*, the antagonist YL-365 doesnot contain hydrophilic head and loses the interactions within the TM bundles. By contrast, the hydrophilic head of LysoPS (18:1) occupies the core region of helical bundles, and connects TM3 with TM5 or TM6 by making direct interactions with $Y135^{3.33}$, $N220^{5.40}$, or $Q293^{6.62}$, which results in notable displacement and inward movement of the residues $N220^{5.40}$ and $Q293^{6.62}$ upon activation (Fig. 4*B*). Moreover, we also noticed that the distance between the critical activation residues $Y135^{3.33}$ and $R286^{6.55}$ decreased upon agonist binding (Fig. 4*B*).

We then inspected critical microswitch residues required for receptor activation. In the activation process of GPR34, the polar interaction between $N220^{5.40}$ and LysoPS (18:1) results in

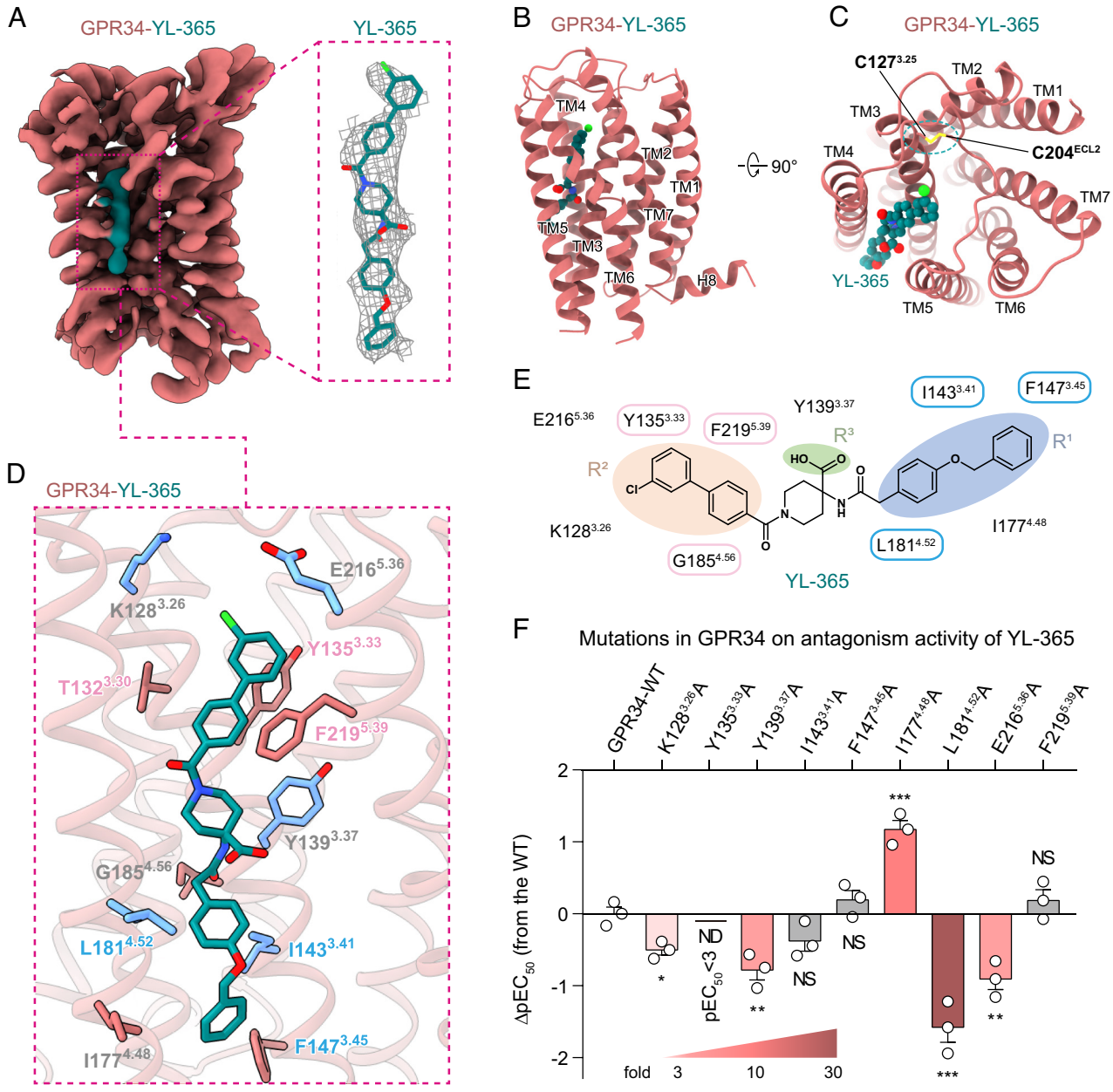


**Fig. 3.** Overall architecture of the inactive GPR34-YL-365 complex. (*A*) Overall cryo-EM structure of GPR34 (light coral)-YL-365(bremen blue) complex. YL-365 is shown as bremen blue stick. (*B*) Cartoon representation of GPR34. YL-365 is shown as bremen blue spheres. (*C*) *Top* views of GPR34-YL-365. The disulfide bond formed between C127$^{3.25}$ and C204$^{ECL2}$ is shown as brilliant yellow stick. (*D*) Overall structure of hydrophobic-binding pocket viewed from the membrane plane, showing interactions between the bound YL-365 and residues in the pocket. Key residues are highlighted as sky blue. (*E*) Chemical structure of the antagonist YL-365 showing the $R^1$, $R^2$ and $R^3$ groups. The key residues forming the hydrophobic interactions between GPR34 and YL-365 are marked with orange and blue circles, respectively. (*F*) Mutagenic effects of the binding pocket residues to YL-365-induced receptor inhibition examined by $G\alpha_{i1}$-$G\gamma_2$ dissociation assay. Bars represent differences in calculated potency ($\Delta pEC_{50}$) for each mutant shown as percentage of the maximum in WT. The $\Delta pEC_{50}$ values were derived from the dose–dependent curves in *SI Appendix*, Fig. S7*E*. Statistical differences between WT and mutants were determined by two-sided, one-way ANOVA with Tukey's test. *$P$ < 0.05; **$P$ < 0.01; ***$P$ < 0.001; ND, not detectable due to low signal; NS, no significant difference. Data are presented as the mean ± SEM of three independent experiments performed in triplicate.

movement of TM5 toward TM6 and rearrangement of F$^{6.48}$ and I$^{5.50}$-I$^{3.40}$-F$^{6.44}$ (I-I-F) motif (*SI Appendix*, Fig. S8*B*). A similar manner was observed in $\beta_2$AR or μOR activation, respectively (40, 41) (*SI Appendix*, Fig. S8*B*). In GPR34, the residue I$^{3.40}$ that undergoes subtle rearrangement forms direct contacts with F$^{6.44}$ and F$^{6.48}$, we next explore the functional role of the residues I$^{3.40}$ as well as I$^{5.50}$ for GPR34 activation, alanine replacements of I$^{3.40}$ and I$^{5.50}$ in GPR34 significantly reduced the receptor activation induced by LysoPS (18:1) (*SI Appendix*, Fig. S8*C*), indicating that these two residues play a critical role in signaling transduction of GPR34. Compared with class A GPCRs, the "toggle switch" residue F$^{6.48}$ of GPR34 is at a lower position than the equivalent residues W$^{6.48}$ in μOR (40, 42) or $\beta_2$AR (41, 43), which is packed against I$^{3.40}$ of the canonical P-I-F microswitch that forms the core triad motif for receptor activation (44) (Fig. 4*C*). Therefore, in the structure of GPR34, F$^{6.48}$ and I$^{5.50}$-I$^{3.40}$-F$^{6.44}$ (I-I-F) together constitutes a core quaternary motif to trigger rearrangement of TM3, TM5, and TM6 synergistically, thus acting as a central hub in responsible to sense ligand as well as induce receptor activation (Fig. 4*C*). The previous literatures have reported that the core quaternary (PIF-W)-like motif in CysLT1R and PAR1, in both structures, the microswitch residue F$^{6.48}$ is located at a lower position in those relative to W$^{6.48}$ in $\beta_2$AR

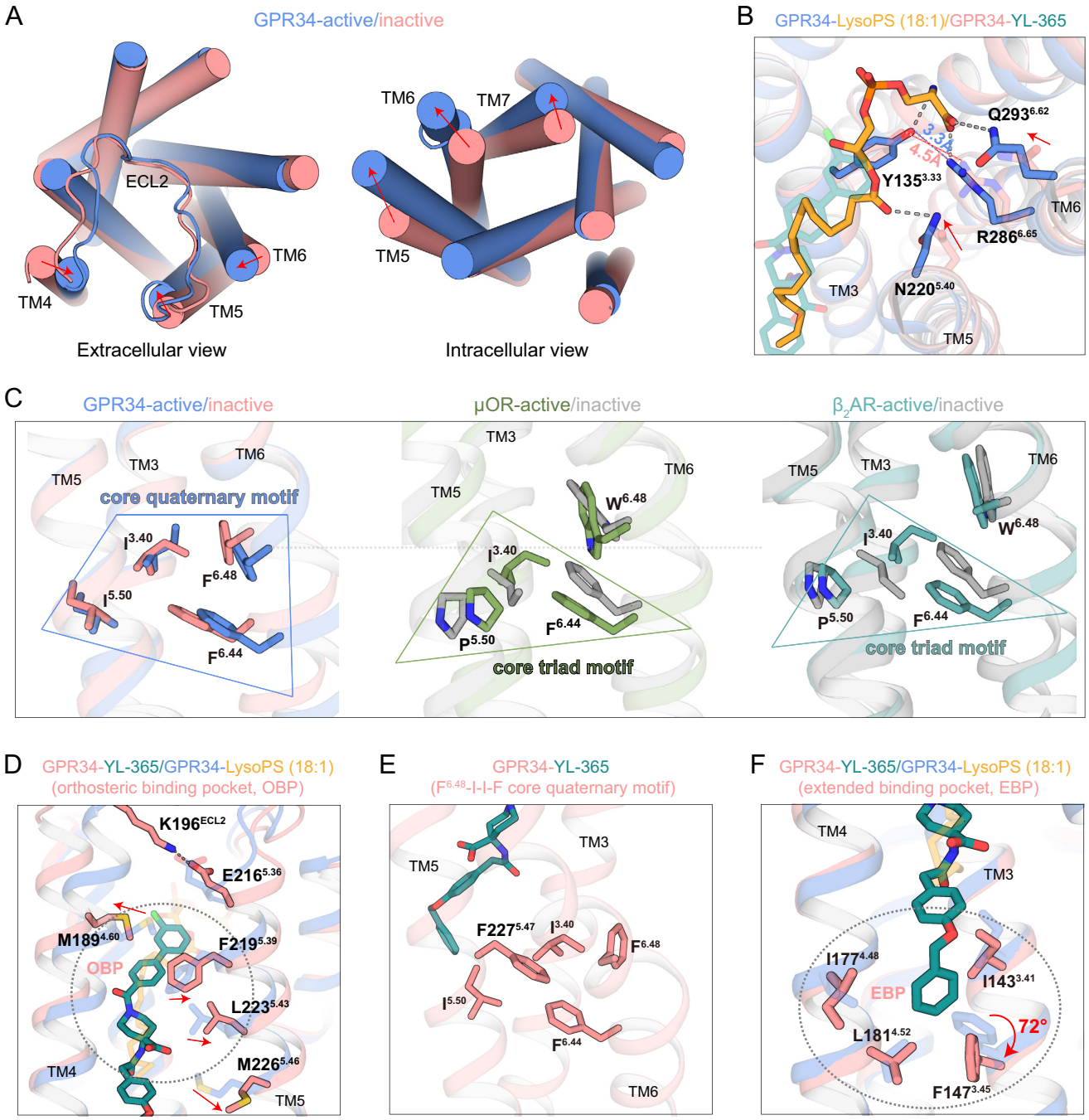


**Fig. 4.** Structural comparison of GPR34 in active state and inactive state. (*A*) Structural superposition of active and inactive GPR34 from the extracellular view (*Left*) and intracellular view (*Right*). Significant conformational changes of TM4, TM5, TM6, and ECL2 in the extracellular domain, as well as TM5, TM6, and TM7 in the intracellular domain were observed. The helical bundles were presented as cylindrical helices. (*B*) Structural superposition of LysoPS (18:1) (bright orange) bound and YL-365 (deep teal) bound GPR34 indicated that polar interactions between hydrophilic head of LysoPS (18:1) and GPR34 connected the core helical bundle TM3, TM5, and TM6. The conformational changes from active to inactive state are indicated as red arrows, and the polar interactions are highlighted with grey dashed lines. (*C*) The $F^{6.48}$ together with $I^{5.50}$-$I^{3.40}$-$F^{6.44}$ (I-I-F) motif in GPR34 form a special core quaternary motif. The inactive μOR (PDB: 4DKL), active μOR (PDB: 7T2G), inactive $\beta_2$AR (PDB: 3NY8) and active $\beta_2$AR (PDB: 3SN6) are used for comparison. (*D*) YL-365 binding-induced conformational change of $M189^{4.60}$, $F219^{5.39}$, $L223^{5.43}$, and $M226^{5.46}$ in the OBP and formation of an ion lock between $E216^{5.36}$ and $K196^{ECL2}$. (*E*) $F227^{5.47}$ contacts with the $F^{6.48}$-I-I-F core quaternary motif in the inactive GPR34. (*F*) 4-benzyloxyphenyl moiety of YL-365 engaged with an extended binding pocket (EBP) formed by $I143^{3.41}$, $F147^{3.45}$, $I177^{4.48}$, and $L181^{4.52}$.

(45, 46) (*SI Appendix*, Fig. S8*D*), and their studies suggest a different activation mechanism. Furthermore, by sequence alignment (*SI Appendix*, Fig. S8*E*), we also found that some receptors with available structures have F at position 6.48, which constitutes a different connector switch, suggesting that GPR34 and these receptors may have similar activation mechanism. Our functional assays indicated that $F^{6.48}$A and $F^{6.44}$A mutation of GPR34 diminished receptor activation, whereas the $F^{6.48}$A-$F^{6.44}$A double mutations nearly impaired receptor activation (*SI Appendix*, Fig. S8*C*). In addition, structural comparison reveals a unique conformation of another critical activation motif $D/N^{7.49}P^{7.50}xxY^{7.53}$ in TM7, especially for the residue $Y^{7.53}$ (*SI Appendix*, Fig. S8*F*). In most of the active state class A GPCRs, $Y^{7.53}$ along with the intracellular part of TM7 shifts toward the core helical bundle to form a polar network with $Y^{5.58}$ and $R^{3.50}$. Remarkably, in LysoPS (18:1)-activated GPR34 structure, the side chain of $Y^{7.53}$ rotated around 120° downward from the inactive state and pointed toward ICL1, leading to outward movement of TM7 instead, a similar noncanonical rotamer of $Y^{7.53}$

was observed in complement receptor C5aR1 (47) (*SI Appendix*, Fig. S8*F*). Overall, all these observations suggest a particular activation mechanism for GPR34.

We subsequently figured out to explore the mechanism of antagonist inhibition. Compared with LysoPS (18:1), YL-365 partially occupies the OBP of GPR34, with $R^2$ and $R^3$ groups overlapping with the acyl chain of LysoPS (18:1) (*SI Appendix*, Fig. S8*G*). Thus, YL-365 can spatially compete with the agonist LysoPS (18:1), resulting in an antagonistic effect in some degree. Notably, the phenyl(piperidin-1-yl) methanone group substitution of acyl chain at YL-365 strongly enhances the interactions within the hydrophobic cleft formed by TM3-5, further pushing the extracellular end of TM4 out by 4.4 Å, thus moving away from TM5 (*SI Appendix*, Fig. S8*G*). Such conformational changes lead to a wider open cleft between TM4 and TM5 in YL-365-bound GPR34 structure. As a result, obvious displacements of $M189^{4.60}$, $F219^{5.39}$, $L223^{5.43}$, and $M226^{5.46}$ were observed (Fig. 4*D*). Subsequently, the alteration of TM5, especially for the aromatic residue $F227^{5.47}$, strength contacts with the $F^{6.48}$-I-I-F core quaternary motif (Fig. 4*E*), which stabilizes the receptor in inactive state. Unexpectedly, an ionic lock between $E216^{5.36}$ and $K196^{ECL2}$ at extracellular tips was observed in the structure of YL-365 bound GPR34 (Fig. 4*D*), which may contribute to retention time of antagonist in orthosteric site, blocking the entry of the endogenous LysoPS (18:1) for receptor activation.

It is also noteworthy that the 4-benzyloxyphenyl moiety ($R^1$) of YL-365 was projected into the intracellular end of TM3 and TM4, engaging with an EBP composed by hydrophobic residues $I143^{3.41}$, $F147^{3.45}$, $I177^{4.48}$ and $L181^{4.52}$ (Fig. 4*F*). The result of cell-based functional assays indicated that the residue $L181^{4.52}$ contributes substantially to antagonism effect of YL-365 (*SI Appendix*, Fig. S8*H*). When further comparing with active GPR34, the aromatic side chain of $F147^{3.45}$ in YL-365-bound state has 72° rotation change (Fig. 4*F*). Such rearrangement allosterically caused slight change at intracellular end of TM3. Particularly, the residue $R152^{3.50}$ from DRY ($D^{3.39}$-$R^{3.50}$-$Y^{3.51}$) motif in TM3 required for receptor activation (48) was observed to form noncanonical interaction with $T264^{6.33}$ in TM6, thus shrinking intracellular pocket with respect to G-protein coupling (*SI Appendix*, Fig. S8*I*). Obviously, these observations indicate a special antagonistic mechanism of YL-365.

**Pharmacological and Toxicological Effects of YL-365.** A previous study has shown that GPR34 was predominantly expressed by microglia in the dorsal horn after spinal nerve injury, which exacerbated neuropathic pain in mice. Therefore, we in this investigation intended to evaluate the therapeutic effect of YL-365 in a mouse model of neuropathic pain, in which the L4 spinal nerve was cut off (Fig. 5*A*). Before performing the in vivo pharmacological experiments, we evaluated the in vitro and in vivo toxicity of YL-365. In the 3-(4,5-dimethylthiazol-2-yl)-2,5-diphenyl-2H-tetrazolium bromide (MTT) assay, YL-365 did not show cytotoxicity against a number of human normal cell lines, including HEK293, LX-2, Beas 2B, and HUVEC ($IC_{50}$ > 100 μM, *SI Appendix*, Table S7). Acute toxicity experiments on C57BL/6J mice showed that no mice died after i.p. (intraperitoneally) (200 mg/kg) treatment with YL-365. In a repeated dose toxicity study, following 14 consecutive days i.p. administration of YL-365 twice per day at the dose of 100 mg/kg, mice did not show noticeable change in body weight (Fig. 5*B*) or any damage in diverse organs (*SI Appendix*, Fig. S9). Considering that GPR34 is also expressed in hematological system, the blood cell counts and other blood parameters were examined, and YL-365 did not show any effects on these blood parameters (Fig. 5 *C*–*G*). All these results indicated low toxicity of YL-365 to mice.

We next evaluated the pharmacokinetic (PK) properties in mice. When administered i.p. (20 mg/kg), YL-365 showed area under the curve values of 6614.77 h*ng/mL (*SI Appendix*, Table S8). The half-life ($T_{1/2}$) and the clearance rate (CL) were 1.315 h and 50.15 mL/min/kg, respectively. These results indicated that YL-365 has good PK properties when i.p. administrated.

Finally, the mouse model of neuropathic pain with the L4 spinal nerve being cut off was used to evaluate the therapeutic effect of YL-365 (Fig. 5*A*). Our results showed that 5, 10, or 20 mg/kg i.p. administration of YL-365 twice per day substantially reduced mechanical allodynia in a dose-dependent manner (Fig. 5*H*). To explore the mechanism underlying the antinociceptive effect of YL-365, we detected the expression level of proinflammatory genes (*IL-6*, *IL-1β* and *iNOS*) in M1 microglia and anti-inflammatory genes (*TIMP1, TGF-β* and *IL-4*) in M2 microglia during neuropathic pain in the spinal cord; M1 and M2 microglia are distinct microglial phenotypes with M1 playing a deleterious role and M2 a neuroprotective role (49, 50). YL-365 evidently down-regulated the expression level of *iNOS* (Fig. 5*I*), but had no or very weak effect on other proinflammatory and anti-inflammatory genes (Fig. 5 *I* and *J*). These findings suggested that YL-365 alleviated hyperalgesia in the mouse model of neuropathic pain via down-regulating the expression of *iNOS* in M1 microglia.

## Discussion

LPLs including LPA, S1P, LPC, and LysoPS, are a group of lipid-signaling molecules that exert their effects via specific GPCRs. LPLs and their corresponding GPCRs are attracting attention due to their important roles in regulating various physiological and pathophysiological processes, such as autoimmune diseases, neurodegenerative diseases, pain, cancer, and inflammation. Among these LPLs/GPCRs, LPA and LPA receptors LPAR1–6, S1P and S1P receptors S1PR1–5, and LPC and LPC receptor GPR119 have been well studied (51–53); LPA receptors and S1P receptors have been identified as disease targets with several drugs targeting these receptors already entering clinical trials or approved for clinical use. However, LysoPS and its cognate GPCRs, including GPR34, GPR174, and P2Y10, have been rarely studied. Little had been known about the molecular mechanism of activation of these GPCRs, and there is a lack of potent and selective antagonists of these receptors. Of them, GPR34 is the first reported LysoPS receptor. Several lines of evidence have suggested pathological roles of GPR34 (12). For example, GPR34 has been found to highly express in microglia and the amount of LysoPS species became obvious in the dorsal horn after sensory nerve injury (5). LysoPS/GPR34 signal exacerbates neuropathic pain and accelerates the phagocytic activity of the cells in mice. GPR34 deficiency suppresses hyperalgesia in the mouse model of neuropathic pain. Nevertheless, whether small molecule antagonists of GPR34 could be used as therapeutical agents are unclear.

To reveal the activation mechanism and provide structural information for antagonist identification, we solved the cryo-EM structure of activated GPR34-$G_i$ complex bound to LysoPS (18:1). Like other LPL receptors (24–26, 53), the ligand-binding pocket of GPR34 can be divided into a hydrophilic head binding site and a hydrophobic groove. In particular, there are some significant differences from these LPL receptors in GPR34 structure. The hydrophilic head of S1P, LPA, or LPC binds into a polar pocket consisting of TM1, TM2, and TM7 in S1PR3, LPAR1, or GPR119. However, LysoPS (18:1)

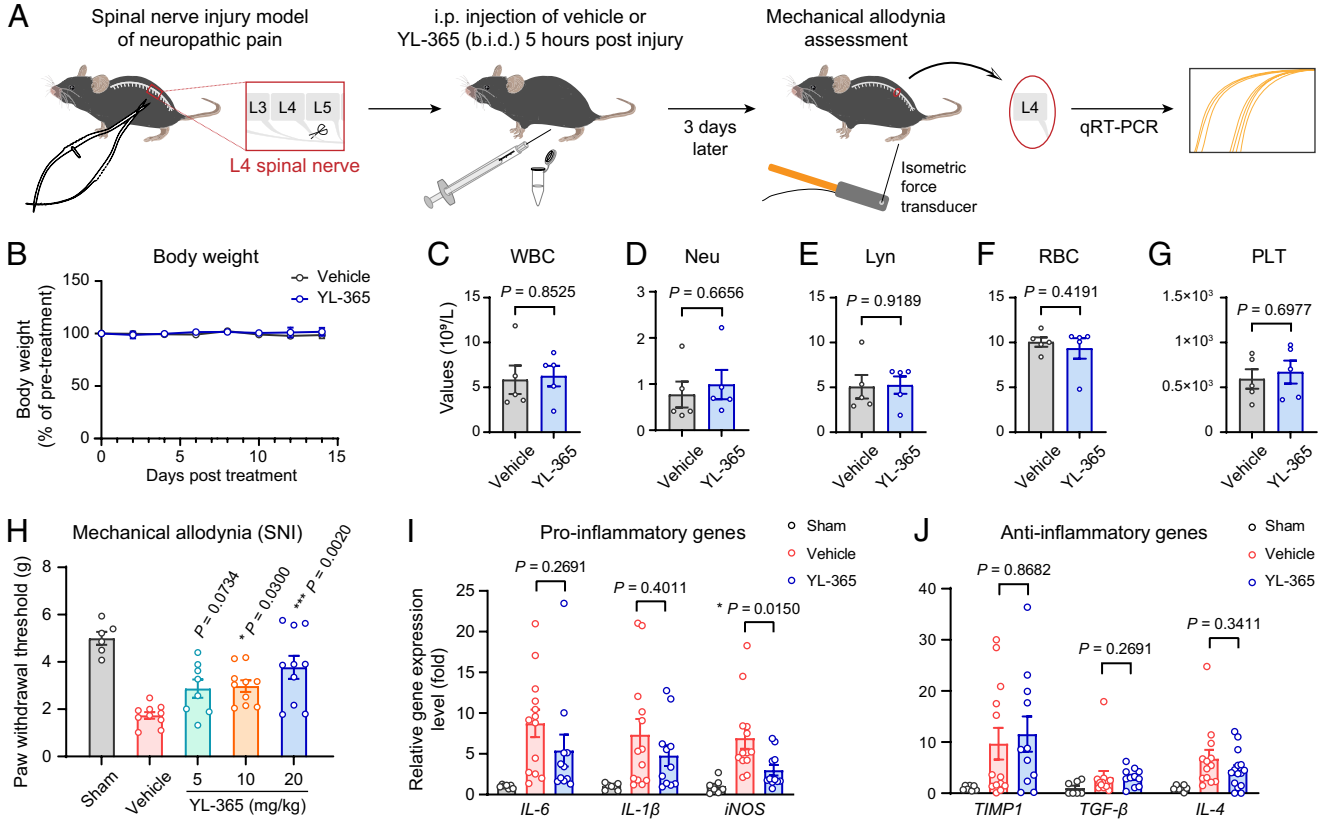


**Fig. 5.** Pharmacological and toxicological effects of YL-365 in vivo. (*A*) The flow diagram of the in vivo antinociceptive experiments of YL-365 in the mouse model of neuropathic pain. (*B*) Body weight variation over time of C57BL/6J mice treated with vehicle or YL-365 (100 mg/kg, i.p., b.i.d.). Data are presented as averages ± SEM of five biological replicates. (*C*–*G*) Complete blood count analyses (white blood cells, neutrophils, lymphocytes, red blood cells, and platelets) and of peripheral blood samples harvested from mice at the end of 14-d treatment with vehicle or YL-365 (100 mg/kg, i.p., b.i.d.). Data are presented as averages ± SEM of five biological replicates. *P* values were analyzed with paired *t* tests. (*H*) Antinociceptive effects of YL-365 in the mouse model of neuropathic pain. Mechanical allodynia was assessed on day 3 in sham-operated (sham) (n = 6) or SNI (spinal nerve injury) mice treated with vehicle or YL-365 (i.p., b.i.d.) (n = 8 to 10). Data are mean ± SEM. The *P* values were analyzed using one-way ANOVA compared with the vehicle group, $*P < 0.05$, $***P < 0.001$. (*I* and *J*) The gene expression level of proinflammatory genes (*I*) and anti-inflammatory genes (*J*) in L4 spinal cord were assessed by qRT-PCR. Data are mean ± SEM (n = 7 for sham group, n = 13 for vehicle and YL-365 (20 mg/kg, i.p., b.i.d.) treatment group). The *P* values were analyzed using one-way ANOVA compared with the vehicle group, $*P < 0.05$, $***P < 0.001$.

occupies the hydrophilic pocket formed by TM3, TM6, and TM7. In addition, the lipid tail of S1P, LPA, or LPC makes engagement with the "toggle switch" residue $W^{6.48}$ in S1PR3 (24), LPAR1 (25) or GPR119 (26). Nevertheless, the binding site of LysoPS (18:1) in GPR34 is 14.4 to 15.8 Å away from the equivalent residue $F^{6.48}$ (*SI Appendix*, Fig. S10*A*). Moreover, N-terminal regions in S1PRs and LPARs fold helical cap that constitutes ligand-binding pocket and were reported to limit access of ligand to the orthosteric site from extracellular region (22, 25, 54, 55) (*SI Appendix*, Fig. S2 *F* and *G*). Instead, the OBP in GPR119 or GPR34 is capped by ECL2 that forms a lid over the extracellular vestibules (*SI Appendix*, Fig. S2 *E* and *H*). Notably, ECL2 regions fold different conformations in two receptors, the lower half of ECL2 in GPR119 folds into a helical turn-like shape and the side chain of $F158^{ECL2}$ is observed to insert into the OBP near TM6, which results in that the hydrophobic tail of LPC inserts deeply into the TM bundle core (*SI Appendix*, Fig. S10*B*). However, the whole ECL2 region of GPR34 folds into a U shape and the side chain of $F205^{ECL2}$ is observed to insert into the pocket, which limits the projection of the hydrophilic head of LysoPS (18:1) toward TM1 and TM2. In addition, the distribution of polar residues in GPR119 or GPR34 is quite different, which results in a distinct binding pose of LPC and LysoPS (18:1) though the chemical structure is similar (*SI Appendix*, Fig. S10*B*). These differences suggest that LPL GPCRs may behave in distinct activation mechanisms in response to their specific ligands.

Combined with structural observation and functional experiments, we revealed that both the hydrophilic and hydrophobic sites were important for GPR34 activation stimulated by LysoPS (18:1). Specially, consistent with previous SAR study (18), our mutagenesis studies further indicated that trimming the length of LysoPS (18:1) undermines activation of GPR34, suggesting that the hydrophobic cleft formed by TM3-5 engaged in LysoPS (18:1) recognition, for instance $Y139^{3.37}$ and $L223^{5.43}$, were necessary to trigger signal transduction (*SI Appendix*, Fig. S3*G*). The distinct architectures of LPL-binding pockets in these lipid receptors appear to have determinant role for specific ligand recognition. More importantly, such unique characteristic of LysoPS (18:1)-bound GPR34 structure would contribute to design therapeutic agents with specific selectivity for diseases treatment.

By utilizing the solved cryo-EM structure of LysoPS (18:1)-bound GPR34, we retrieved an antagonist, Hit-1. Here one may wonder why the agonist-bound active GPR34 structure was used for molecular docking, but an antagonist was obtained. In fact, the molecule we obtained can efficiently occupy the OBP of GPR34, hence preventing the agonist binding. In addition, the polar interaction network formed between the agonist and TM3/6/7 (residues $Y135^{3.33}$, $R286^{6.55}$, $Y289^{6.58}$ and $N309^{7.35}$) has been demonstrated to play a key determinant role in the

activation of LysoPS receptor subfamily (18, 27). In order to retrieve antagonists, we have already filtered out molecules that might have potential to form such polar interaction network when we selected candidate molecules after molecular docking (*SI Appendix, Methods* section), indicating that the selected molecules do not have the ability to active the receptor. Subsequent structural optimization toward Hit-1 offered a highly potent and selective GPR34 antagonist, YL-365. Structural determination of GPR34 in complex YL-365 revealed a binding site, including partial OBP and EBP, between TM3-TM5. YL-365 occupies partially the orthosteric site, thereby competitively inhibiting LysoPS (18:1)-induced activation. On the other hand, the 4-benzyloxyphenyl moiety extended into the EBP region and allosterically affected the conformational rearrangement of $R^{3.50}$ in the DRY motif, which is an important switch for activation or inhibition in GPCRs. In detail, in the structure of LysoPS (18:1)-bound GPR34, $R152^{3.50}$ in the DRY motif forms hydrogen bonds with $Y238^{5.58}$ in TM5 to stabilize the active state. However, in the antagonist YL-365-bound structure, the conformational changes switch the interaction from $R152^{3.50}$-$Y238^{5.58}$ to $R152^{3.50}$-$T264^{6.33}$, stabilizing the inactive state of GPR34 (*SI Appendix*, Fig. S8*E*). Particularly, structural comparison of active with inactive states reveals that $F^{6.48}$ and I-I-F in the connector layer of receptor forms a core quaternary motif, which acts as a central hub to induce rearrangement TM5 and TM6 and receptor activation (Fig. 4*C*).

The identified GPR34 antagonist YL-365 showed potent activity against GPR34 with an $IC_{50}$ value of 17 nM. This compound displayed excellent selectivity for GPR34 against other LPL receptors and protein kinases and exhibited favorable PK properties. In a mouse model of neuropathic pain, YL-365 displayed outstanding antinociceptive effect, but did not show obvious toxicity. Mechanism studies indicated that YL-365 treatment down-regulated the expression of *iNOS* in M1 microglia, hence suppressing proinflammatory responses of microglia and alleviating hyperalgesia.

In summary, we solved the cryo-EM structures of both activated and inactivated GPR34, and provided mechanistic insights into the GPR34 activation and antagonist inhibition. Structure characteristics of GPR34 reveal an unusual activation mechanism, and the unexpected hydrophobic cleft of TM3-TM5 for ligand recognition offers an opportunity for antagonist identification. By utilizing the structure of GPR34, we identified a potent and selective GPR34 antagonist and have demonstrated its efficacy in the neuropathic pain model. Our findings highlight a great potential of GPR34 antagonists in disease treatment. This study will undoubtedly start the upsurge of drug identification targeting LysoPS receptors.

## Materials and Methods

Detailed description of cryo-EM sample preparation and data collection, molecular docking, molecular dynamics simulations, Tango assay, BRET-based $G\alpha_{i1}$-$\gamma_2$ dissociation assay, enzyme-linked immunosorbent assay, TGF-α shedding assay, GloSensor assay, IP-1 detection assay, NanoBiT luciferase assay, kinase profiling assay, MTT assay, PK analysis, toxicity study, quantitative real-time PCR and in vivo neuropathic pain experiment are provided in *SI Appendix*.

**Cell Culture.** Unless specifically mentioned, cell lines used in this study were obtained from the American Type Culture Collection (ATCC), Cell Bank of Chinese Academy of Sciences. HEK-293 (ATCC), HEK293T (ATCC), LX-2 (Merck), Beas 2B (Cell Bank of Chinese Academy of Sciences) and HUVEC (ATCC) cells were cultured in Dulbeccos Modified Eagle Medium (DMEM) (Gibco) supplemented with 10% fetal bovine serum (FBS) (Cell-Box), 100 U/mL penicillin and 100 μg/mL streptomycin (Hyclone, SV30010). CHO-K1 cells (Cell Bank of Chinese Academy of Sciences) were cultured in DMEM/F12 medium (Gbico) supplemented with 10% FBS ||(Cell-Box), 100 U/mL penicillin and 100 μg/mL streptomycin (Hyclone, SV30010). HTLA cells were maintained in DMEM supplemented with 10% FBS, 100 U/mL penicillin, 100 μg/mL streptomycin, 2 μg/mL puromycin, and 100 μg/mL hygromycin B. All cells were grown in a humidified incubator at 37 °C with 5% $CO_2$.

**Animals.** The animals used in this study were all purchased from Gempharmatech Co. Ltd (Gempharmatech Co. Ltd) and maintained on a 12:12 light–dark cycle at a room temperature of 22 ± 1 °C.

**Statistical Analysis.** All data were analyzed with GraphPad Prism 8.0 software. Statistical comparison between different groups was performed by one-way ANOVA, paired two-tailed Student's *t* test. Differences were considered statistically significant when $P < 0.05$.

**Inclusion and Ethics Statement.** This research posed no health, safety, security, or other risk to researchers. The animal experiments were approved by the Institutional Animal Care and Use Committee, West China Hospital, Sichuan University (Permit Number: 20211016006). All animal experimental procedures were conducted in accordance with the Regulations for the Administration of Affairs Concerning Experimental Animals approved by the State Council of People's Republic of China.

**Data, Materials, and Software Availability.** Coordinates and cryo-EM maps data have been deposited in Protein Data Bank (PDB) and Electron Microscopy Data Bank (EMDB) (PDB: 8SAI (56) and 8IYX (57) EMDB: EMDB-40270 (58) and EMDB-35832 (59)).

**ACKNOWLEDGMENTS.** Cryo-EM data for GPR34-LysoPS (18:1)-$G_i$ complex were collected at Cryo-EM Center in Southern University of Science and Technology. Cryo-EM data for GPR34-YL365 complex were collected at the State Key Laboratory of Biotherapy (SKLB) West China Cryo-EM Center in Sichuan University. All Cryo-EM data were processed at SKLB Duyu High Performance Computing Centre in Sichuan University. This work was supported by National Natural Science Foundation of China (81930125, T2221004 and 82130104 to S.Y.; 31972916 to Z. Shao; 81971974 to H.D.; 81821001 and 82130107 to R.Z.; 32222040 to Z. Su; 82103974 to A.X.; and 22277085 to X.Y.); Ministry of Science and Technology of China (2019YFA0508800 to Z. Shao; 2021YFA1301900 to H.D.; 2019YFA0508500 to R.Z.; and 2022YFC2303700 and 2021YFA1301900 to Z. Su); Science and Technology department of Sichuan Province (2022ZYD0085 to Z. Shao; and 2021ZYD0080 to W.Y.); the Frontiers Medical Center, Tianfu Jincheng Laboratory Foundation (TFJC2023010009 to S.Y.; and TFJC2023010010 to Z. Shao); 1.3.5 Project for Disciplines of Excellence, West China Hospital, Sichuan University (ZYXY21001 and ZYGD18001 to S.Y.; ZYYC20023 to Z. Shao; and ZYYC20021 to H.D.); and the Chinese Academy of Sciences Project for Young Scientists in Basic Research (YSBR-074 to R.Z.).

Author affiliations: [a]Department of Biotherapy, Cancer Center and Kidney Research Institute, State Key Laboratory of Biotherapy and National Clinical Research Center for Geriatrics, West China Hospital, Sichuan University, Chengdu, Sichuan 610041, China; [b]Department of Ophthalmology and Research Laboratory of Macular Disease, West China Hospital, Sichuan University, Chengdu, Sichuan 610041, China; [c]The Chinese Academy of Sciences Key Laboratory of Innate Immunity and Chronic Disease, School of Basic Medical Sciences, Division of Life Sciences and Medicine, University of Science and Technology of China, Hefei, Anhui 230027, China; [d]Institute of Health and Medicine, Hefei Comprehensive National Science Center, Hefei, Anhui 230601, China; [e]Key Laboratory of Drug Targeting and Drug Delivery System of Ministry of Education, West China School of Pharmacy, Sichuan University, Chengdu, Sichuan 610041, China; and [f]Frontier Medical Center Tianfu Jincheng Laboratory, Chengdu, Sichuan 610212, China

1. K. Makide, H. Kitamura, Y. Sato, M. Okutani, J. Aoki, Emerging lysophospholipid mediators, lysophosphatidylserine, lysophosphatidylthreonine, lysophosphatidylethanolamine and lysophosphatidylglycerol. *Prostaglandins Other Lipid Mediat.* **89**, 135–139 (2009).
2. F. Bellini, A. Bruni, Role of a serum phospholipase A1 in the phosphatidylserine-induced T cell inhibition. *FEBS Lett.* **316**, 1–4 (1993).
3. X. Wang *et al.*, GPR34-mediated sensing of lysophosphatidylserine released by apoptotic neutrophils activates type 3 innate lymphoid cells to mediate tissue repair. *Immunity* **54**, 1123–1136.e8 (2021).
4. L. Lou *et al.*, Mafba and Mafbb regulate microglial colonization of zebrafish brain via controlling chemotaxis receptor expression. *Proc. Natl. Acad. Sci. U.S.A.* **119**, e2203273119 (2022).

5. A. Sayo *et al.*, GPR34 in spinal microglia exacerbates neuropathic pain in mice. *J. Neuroinflammation* **16**, 1–11 (2019).
6. M. J. Barnes *et al.*, The lysophosphatidylserine receptor GPR174 constrains regulatory T cell development and function. *J. Exp. Med.* **212**, 1011–1020 (2015).
7. M. Gurusamy *et al.*, G-protein-coupled receptor P2Y10 facilitates chemokine-induced CD4 T cell migration through autocrine/paracrine mediators. *Nat. Commun.* **12**, 6798 (2021).
8. T. Sugo *et al.*, Identification of a lysophosphatidylserine receptor on mast cells. *Biochem. Biophys. Res. Commun.* **341**, 1078–1087 (2006).
9. A. Inoue *et al.*, TGFα shedding assay: An accurate and versatile method for detecting GPCR activation. *Nat. Methods* **9**, 1021–1029 (2012).
10. H. Kitamura *et al.*, GPR34 is a receptor for lysophosphatidylserine with a fatty acid at the sn-2 position. *J. Biochem.* **151**, 511–518 (2012).
11. A. Bédard, P. Tremblay, A. Chernomoretz, L. Vallières, Identification of genes preferentially expressed by microglia and upregulated during cuprizone-induced inflammation. *Glia* **55**, 777–789 (2007).
12. T. Schoeneberg, J. Meister, A. B. Knierim, A. Schulz, The G protein-coupled receptor GPR34–the past 20 years of a grownup. *Pharmacol. Ther.* **189**, 71–88 (2018).
13. Z.-T. Jin *et al.*, G-protein coupled receptor 34 knockdown impairs the proliferation and migration of HGC-27 gastric cancer cells in vitro. *Chin. Med. J. (Engl).* **128**, 545–549 (2015).
14. Y. Iida *et al.*, Lysophosphatidylserine stimulates chemotactic migration of colorectal cancer cells through GPR34 and PI3K/Akt pathway. *Anticancer Res.* **34**, 5465–5472 (2014).
15. B. Zuo *et al.*, G-protein coupled receptor 34 regulates the proliferation and growth of LS174T cells through differential expression of PI3K subunits and PTEN. *Mol. Biol. Rep.* **49**, 2629–2639 (2022).
16. Y. Tan, H. Wang, C. Zhang, MicroRNA-381 targets G protein-Coupled receptor 34 (GPR34) to regulate the growth, migration and invasion of human cervical cancer cells. *Environ. Toxicol. Pharmacol.* **81**, 103514 (2021).
17. I. Liebscher *et al.*, Altered immune response in mice deficient for the G protein-coupled receptor GPR34. *J. Biol. Chem.* **286**, 2101–2110 (2011).
18. M. Ikubo *et al.*, Structure–activity relationships of lysophosphatidylserine analogs as agonists of G-protein-coupled receptors GPR34, P2Y10, and GPR174. *J. Med. Chem.* **58**, 4204–4219 (2015).
19. S. Jung *et al.*, Conformational constraint of the glycerol moiety of lysophosphatidylserine affords compounds with receptor subtype selectivity. *J. Med. Chem.* **59**, 3750–3776 (2016).
20. M. Sayama *et al.*, Probing the hydrophobic binding pocket of g-protein-coupled lysophosphatidylserine receptor GPR34/LPS1 by docking-aided structure–activity analysis. *J. Med. Chem.* **60**, 6384–6399 (2017).
21. S. Nakamura *et al.*, Non-naturally occurring regio isomer of lysophosphatidylserine exhibits potent agonistic activity toward G protein-coupled receptors. *J. Med. Chem.* **63**, 9990–10029 (2020).
22. Y. Yuan *et al.*, Structures of signaling complexes of lipid receptors S1PR1 and S1PR5 reveal mechanisms of activation and drug recognition. *Cell Res.* **31**, 1263–1274 (2021).
23. Y. Kang *et al.*, Cryo-EM structure of human rhodopsin bound to an inhibitory G protein. *Nature* **558**, 553–558 (2018).
24. L. Cheng *et al.*, A pipeline to investigate the structures and signaling pathways of sphingosine 1-phosphate receptors. *J. Vis. Exp.* **184**, e64054 (2022).
25. S. Liu *et al.*, Differential activation mechanisms of lipid GPCRs by lysophosphatidic acid and sphingosine 1-phosphate. *Nat. Commun.* **13**, 731 (2022).
26. P. Xu *et al.*, Structural identification of lysophosphatidylcholines as activating ligands for orphan receptor GPR119. *Nat. Struct. Mol. Biol.* **29**, 863–870 (2022).
27. A. Uwamizu *et al.*, Lysophosphatidylserine analogues differentially activate three LysoPS receptors. *J. Biochem.* **157**, 151–160 (2015).
28. T. Sterling, J. J. Irwin, ZINC 15–Ligand discovery for everyone. *J. Chem. Inf. Model.* **55**, 2324–2337 (2015).
29. G. Barnea *et al.*, The genetic design of signaling cascades to record receptor activation. *Proc. Natl. Acad. Sci. U.S.A.* **105**, 64–69 (2008).
30. K. Zhang, H. Wu, N. Hoppe, A. Manglik, Y. Cheng, Fusion protein strategies for cryo-EM study of G protein-coupled receptors. *Nat. Commun.* **13**, 4366 (2022).
31. G. Pintilie *et al.*, Measurement of atom resolvability in cryo-EM maps with Q-scores. *Nat. Methods* **17**, 328–334 (2020).
32. A. Venkatakrishnan *et al.*, Molecular signatures of G-protein-coupled receptors. *Nature* **494**, 185–194 (2013).
33. K. A. Jacobson *et al.*, Update of P2Y receptor pharmacology: IUPHAR review 27. *Br. J. Pharmacol.* **177**, 2413–2433 (2020).
34. D. Zhang *et al.*, Two disparate ligand-binding sites in the human P2Y1 receptor. *Nature* **520**, 317–321 (2015).
35. K. Zhang *et al.*, Structure of the human P2Y12 receptor in complex with an antithrombotic drug. *Nature* **509**, 115–118 (2014).
36. V. Cherezov *et al.*, High-resolution crystal structure of an engineered human β2-adrenergic G protein-coupled receptor. *Science* **318**, 1258–1265 (2007).
37. L. Shi *et al.*, β2 adrenergic receptor activation: Modulation of the proline kink in transmembrane 6 by a rotamer toggle switch. *J. Biol. Chem.* **277**, 40989–40996 (2002).
38. T. W. Schwartz *et al.*, Molecular mechanism of 7TM receptor activation–A global toggle switch model. *Annu. Rev. Pharmacol. Toxicol.* **46**, 481–519 (2006).
39. B. Holst *et al.*, A conserved aromatic lock for the tryptophan rotameric switch in TM-VI of seven-transmembrane receptors 2. *J. Biol. Chem.* **285**, 3973–3985 (2010).
40. Q. Qu *et al.*, Insights into distinct signaling profiles of the μOR activated by diverse agonists. *Nat. Chem. Biol.* **19**, 423–430 (2022).
41. S. G. Rasmussen *et al.*, Crystal structure of the β2 adrenergic receptor–Gs protein complex. *Nature* **477**, 549–555 (2011).
42. A. Manglik *et al.*, Crystal structure of the μ-opioid receptor bound to a morphinan antagonist. *Nature* **485**, 321–326 (2012).
43. D. Wacker *et al.*, Conserved binding mode of human β2 adrenergic receptor inverse agonists and antagonist revealed by X-ray crystallography. *J. Am. Chem. Soc.* **132**, 11443–11445 (2010).
44. S. G. Rasmussen *et al.*, Crystal structure of the human β2 adrenergic G-protein-coupled receptor. *Nature* **450**, 383–387 (2007).
45. A. Luginina *et al.*, Structure-based mechanism of cysteinyl leukotriene receptor inhibition by antiasthmatic drugs. *Sci. Adv.* **5**, eaax2518 (2019).
46. C. Zhang *et al.*, High-resolution crystal structure of human protease-activated receptor 1. *Nature* **492**, 387–392 (2012).
47. Y. Feng *et al.*, Mechanism of activation and biased signaling in complement receptor C5aR1. *Cell Res.* **33**, 312–324 (2023).
48. G. E. Rovati, V. Capra, R. R. Neubig, The highly conserved DRY motif of class AG protein-coupled receptors: Beyond the ground state. *Mol. Pharmacol.* **71**, 959–964 (2007).
49. R. Orihuela, C. A. McPherson, G. J. Harry, Microglial M1/M2 polarization and metabolic states. *Br. J. Pharmacol.* **173**, 649–665 (2016).
50. N. Kiguchi, D. Kobayashi, F. Saika, S. Matsuzaki, S. Kishioka, Pharmacological regulation of neuropathic pain driven by inflammatory macrophages. *Int. J. Mol. Sci.* **18**, 2296 (2017).
51. K. Yanagida, W. J. Valentine, Druggable lysophospholipid signaling pathways. *Adv. Exp. Med. Biol.* **1274**, 137–176 (2020).
52. Y. Kihara, H. Mizuno, J. Chun, Lysophospholipid receptors in drug discovery. *Exp. Cell Res.* **333**, 171–177 (2015).
53. J. Liang *et al.*, Structural basis of lysophosphatidylserine receptor GPR174 ligand recognition and activation. *Nat. Commun.* **14**, 1012 (2023).
54. C. Zhao *et al.*, Structural insights into sphingosine-1-phosphate recognition and ligand selectivity of S1PR3–Gi signaling complexes. *Cell Res.* **32**, 218–221 (2022).
55. M. A. Hanson *et al.*, Crystal structure of a lipid G protein–coupled receptor. *Science* **335**, 851–855 (2012).
56. X. Yong *et al.*, 8SAI, Cryo-EM structure of GPR34-Gi complex. Protein Data Bank. https://www.rcsb.org/structure/unreleased/8SAI. Deposited 1 April 2023.
57. G. Jia *et al.*, 8IYX, Cryo-EM structure of the GPR34 receptor in complex with the antagonist YL-365. Protein Data Bank. https://www.rcsb.org/structure/unreleased/8IYX. Deposited 6 April 2023.
58. X. Yong *et al.*, EMD-40270, Cryo-EM structure of GPR34-Gi complex. Electron Microscopy Data Bank. https://www.ebi.ac.uk/emdb/EMD-40270. Deposited 1 April 2023.
59. G. Jia *et al.*, EMD-35832 Cryo-EM structure of the GPR34 receptor in complex with the antagonist YL-365. Electron Microscopy Data Bank. https://www.ebi.ac.uk/emdb/EMD-35832. Deposited 6 April 2023.